

Remote sensing inversion and spatial variation of land surface temperature over mining areas of Jixi, Heilongjiang, China

Jia-shuo Cao^{1,2}, Zheng-yu Deng^{1,2}, Wen Li^{Corresp., 1}, Yuan-dong Hu^{1,2}

¹ College of Landscape Architecture, Northeast Forestry University, Harbin, Heilongjiang, China

² Key Laboratory for Garden Plant Germplasm Development & Landscape Eco-Restoration in Cold Regions of Heilongjiang Province, Harbin, Heilongjiang, China

Corresponding Author: Wen Li
Email address: liwen@nefu.edu.cn

Background. Jixi is a typical mining city in China that has undergone dramatic changes in its land-use pattern of mining areas over the development of its coal resources. Impacts of coal mining activities have greatly affected the regional land surface temperature and ecological system.

Methods. The Landsat 8 Operational Land Imager (OLI) data from 2015 and 2019 were used from the Jiguan, Didao, and Chengzihe District of Jixi in Heilongjiang, China as the study area. The calculations to determine the land-use classification, vegetation coverage, and land surface temperature (LST) were performed using ArcGIS10.5 and ENVI 5.3 software packages. A correlation analysis revealed the impact of land-use type, vegetation coverage, and coal mining activities on LSTs.

Results. The results show significant spatial differentiation in the LSTs of Jixi City. The LSTs for various land-use types were ranked from high to low as follows: mining land > construction land > grassland > cultivated land > forest land > water area. The LST was lower in areas with high vegetation coverage than in other areas. For every 0.1 increase in vegetation coverage, the LST is expected to drop by approximately 0.75 °C. An analysis of mining land patches indicates that the patch area of mining lands has a significant positive correlation with both the average and maximum patch temperatures. The average patch temperature shows a logarithmic increase with the growth of the patch area, and within 200,000 m², the average patch temperature increases significantly. The maximum patch temperature shows a linear increase with the patch area growth, and for every 100,000 m² increase in the patch area of mining lands, the maximum patch temperature increases by approximately 0.81 °C. The higher the average patch temperature of mining land, the higher the temperature in its buffer zone, and the greater its influence scope. This study provides a useful reference for exploring the warming effects caused by coal mining activities and the definition of its influence scope.

1 Remote Sensing Inversion and Spatial Variation of 2 Land Surface Temperature over Mining Areas of Jixi, 3 Heilongjiang, China

4

5 Jia-shuo Cao^{1,2}, Zheng-yu Deng^{1,2}, Wen Li¹, Yuan-dong Hu^{1,2}

6

7 ¹College of Landscape Architecture, Northeast Forestry University, Harbin, Heilongjiang, China8 ²Key Laboratory for Garden Plant Germplasm Development & Landscape Eco-Restoration in

9 Cold Regions of Heilongjiang Province, Harbin, Heilongjiang, China

10

11 Corresponding Author:

12 Wen Li

13 Northeast Forestry University, 26 Hexing Road, Harbin, Heilongjiang, 150040, China

14 Email address: liwen@nefu.edu.cn

15

16 Abstract

17 **Background.** Jixi is a typical mining city in China that has undergone dramatic changes in its
18 land-use pattern of mining areas over the development of its coal resources. Impacts of coal
19 mining activities have greatly affected the regional land surface temperature and ecological
20 system.

21 **Methods.** The Landsat 8 Operational Land Imager (OLI) data from 2015 and 2019 were used
22 from the Jiguan, Didao, and Chengzihe District of Jixi in Heilongjiang, China as the study area.
23 The calculations to determine the land-use classification, vegetation coverage, and land surface
24 temperature (LST) were performed using ArcGIS 10.5 and ENVI 5.3 software packages. A
25 correlation analysis revealed the impact of land-use type, vegetation coverage, and coal mining
26 activities on LSTs.

27 **Results.** The results show significant spatial differentiation in the LSTs of Jixi City. The LSTs
28 for various land-use types were ranked from high to low as follows: mining land > construction
29 land > grassland > cultivated land > forest land > water area. The LST was lower in areas with
30 high vegetation coverage than in other areas. For every 0.1 increase in vegetation coverage, the
31 LST is expected to drop by approximately 0.75 °C. An analysis of mining land patches indicates
32 that the patch area of mining lands has a significant positive correlation with both the average
33 and maximum patch temperatures. The average patch temperature shows a logarithmic increase
34 with the growth of the patch area, and within 200,000 m², the average patch temperature
35 increases significantly. The maximum patch temperature shows a linear increase with the patch
36 area growth, and for every 100,000 m² increase in the patch area of mining lands, the maximum
37 patch temperature increases by approximately 0.81 °C. The higher the average patch temperature
38 of mining land, the higher the temperature in its buffer zone, and the greater its influence scope.

39 This study provides a useful reference for exploring the warming effects caused by coal mining
40 activities and the definition of its influence scope.

41

42 **Introduction**

43 The land surface temperature (LST) comprehensively reflects the energy exchange between land
44 and the atmosphere, which is an important geophysical parameter in the ground-air system (Li et
45 al., 2016; Zhu et al., 2016). Coupling the inversion results of LST with other parameters, such as
46 land-use type and vegetation coverage, provides a scientific basis for ecological environmental
47 protection (Li et al., 2014; Liang, & Zhai, 2014; Xu, He & Huang, 2013; Zhang et al., 2013). The
48 commonly used LST inversion algorithms are divided primarily into the single-channel
49 algorithm, multi-channel algorithm, and split-window algorithm (Zhu et al., 2016). Among them,
50 the single-channel algorithms include the atmospheric correction method, Mono-window
51 algorithm, and the Jiménez-Muñoz J.C single-channel algorithm (Qin, Karnieli & Berliner, 2001;
52 Jiménez-Muñoz et al., 2008). The multi-channel algorithms mainly include the day-night method,
53 temperature emissivity separation algorithm, and graybody emissivity method (Gan et al., 2006;
54 Gillespie, Rokugawa & Matsunaga, 2002; Zhang et al., 2000). The split window algorithm is
55 based mostly on data from the Landsat-TIRS, NOAA-AVHRR, and TERRA-MODIS
56 (Rozenstein et al., 2014; Qin & Karnieli, 2011; Mao et al., 2005).

57 Due to aggravation of the heat island effect, current research on LSTs is mostly focused on
58 urban areas. Analyzing differences in LSTs for different land-use types optimizes the distribution
59 of green space from the perspective of landscape patterning to reduce the heat island effect (Liu,
60 2016). However, mining areas, which are often affected by high temperatures and cause safety
61 problems, have not attracted sufficient attention and are rarely studied.

62 Some research has shown that in the resource development process for resource-based cities,
63 the land-use patterns in mining areas are constantly changing, which causes a series of impacts
64 on the regional ecological environment (Li et al., 2018; Chabukdhara & Singh, 2016; Xie et al.,
65 2011). Therefore, research focusing on coupling between land-use patterns in mining areas and
66 the ecological environment indicators, such as the LST, water environment quality, and
67 biodiversity, has become vital to environmental sustainability (Zhou & Wang, 2014; Xiao, Hu &
68 Fu, 2014; Hu, Duo & Wang, 2018; Bian et al., 2018). Current research on land surface
69 temperatures in mining areas mainly includes the temporal and spatial distribution characteristics
70 of the surface temperature, the impact of ecological disturbance on the surface temperature, and
71 others, where the scales are mostly at macro-regions (Li, Yang & Lei, 2017; Qiu & Hou, 2013;
72 Xie et al., 2011;). This study specifically analyzes the overall and local distribution
73 characteristics of LSTs from smaller scales to explore the radius of influence of high-temperature
74 points. This provides a reference to establish heat alerts in mining areas.

75 Jixi is a typical mining city in China that has undergone dramatic changes in its land-use
76 pattern in the mining area during the development of coal resources. Significant amounts of
77 cultivated land, forest land, and other land types have been replaced by industrial and mining
78 sites, which has greatly affected the regional ecological environment. Impacts such as the
79 atmospheric diffusion of pollutants and the rise of LSTs have affected the regional landscape and
80 ecological systems (Pan et al., 2013; Liao, 2009). This paper uses data from the Landsat 8 OLI
81 remote sensing images from 2015 and 2019 to determine LSTs using the radiation conduction
82 equation over the study area, which encompasses the Jiguan, Didao, and Chengzihe District of
83 Jixi. We analyzed the spatial differentiation and correlations of the LST with the land-use type
84 and vegetation coverage to provide a theoretical framework to reduce the heat island effects
85 caused by local urban development and coal mining activities.

86

87 **Materials & Methods**

88 **Overview of the study area**

89 The study area encompasses the Jiguan, Didao, and Chengzihe District of Jixi, which are the
90 main mining lands with a total area of 827.87 km². Jixi is located in the southeast of
91 Heilongjiang Province, between 130°24'24"–133°56'30" E, 44°51'12"–46°36'55" N. To the
92 southeast and across the ocean in Russia, while to the west and south are Mudanjiang, and to the
93 north is Qitaihe (Fig. 1). The province comprises Mishan, Hulin, and Jidong Counties and six
94 other districts (Jiguan, Hengshan, Didao, Chengzihe, Lishu, and Mashan). The study area is part
95 of the cold-temperate continental monsoon climate, where the average annual temperature is 3.7
96 °C, the average precipitation is 537.5 mm, the annual sunshine is 2709 h and the average frost-
97 free period is 140 d. The terrain is composed primarily of mountains, hills and plains.

98 Jixi is relatively rich in mineral resources with multiple mining areas. However, there also are
99 several abandoned mines that severely damage the ecological environment. In addition, urban
100 construction and industrial development have encroached on grasslands, woodlands, and
101 wetlands, which increases the ecological vulnerability and risks in these ecosystems (He, 2010).

102

103 **Data sources and preprocessing treatments**

104 This paper is based on the Landsat 8 OLI remote sensing images from 2015 and 2019, all of
105 which are from the US Geological Survey (<http://glovis.usgs.gov/>). All images have a spatial
106 resolution of 30 m. The image strip numbers/rows used in this study are 115/28 and 115/29,
107 respectively, and the imaging time was from July to September. Cloud cover in these images was
108 less than 2%, and they were interpreted and classified based on a series of preprocessing
109 treatments, including radiation calibration, atmospheric correction, band synthesis and image
110 cropping.

111

112 Analytical methods

113 The spatial differentiation characteristics of the LST in the Jiguan, Didao, and Chengzihe
114 Districts of Jixi were used to identify heat islands and their influencing factors. We selected a
115 single-window algorithm for inversion of the LSTs. These results were used to analyze the
116 effects of the land-use type, vegetation coverage and coal mining activities on the spatial
117 distribution of LSTs.

118 Determining land-use classification and vegetation coverage

119 Land use is the most direct manifestation of the interaction between human activities and the
120 natural environment as it reflects this close relationship in both time and space (Mooney,
121 Duraiappah & Larigauderie, 2013; Liu et al., 2014). Typically, areas designated as land resources
122 reflects the status of natural resources within the study area. Changes in land-use patterns
123 inevitably cause changes in the LSTs and ecosystem functionality. Therefore, the study of land
124 use is of great importance for regional ecological analyses (Marceau et al., 2003).

125 The relationship between vegetation coverage and the LST has become a focus of research on
126 heat islands (Wang et al., 2011). Green vegetation affects LSTs through photosynthesis,
127 transpiration and evapotranspiration. Ma et al. (2010) compared and analyzed five correlation
128 degrees among planting parameters and LSTs, including the normalized difference vegetation
129 index (NDVI), ratio vegetation index (RVI), greenness vegetation index (GVI), modified soil to
130 adjust vegetation index (MSAVI) and vegetation coverage. They concluded that the correlation
131 between vegetation coverage and the LST was both high and stable because it is not markedly
132 influenced by spatial location or changes in the fraction or type of surface coverage. Therefore,
133 the relationship between vegetation coverage and the LST was selected to study heat island
134 effects within different land surfaces.

135 Land-use classification

136 The ENVI 5.3.1 (L3Harris Geospatial Solutions, Inc., Melbourne, FL, USA) and ArcGIS 10.5
137 (Esri, Corp., Redlands, CA, USA) were used to preprocess the original image data, which
138 includes geometric correction, mosaic compilation, fusion, clipping, research scope extraction,
139 image enhancement and supervised classification, before interpreting and analyzing the remote
140 sensing imagery. The classification of land-use types in the study area was consistent with the
141 standard land-use classification (GB/T 21010–2017). The study area was divided into six
142 categories: forest lands, grasslands, construction lands, cultivated lands, mining lands and water
143 areas. A maximum-likelihood approach was used for the classification. In the final stage of the
144 study, the remote sensing image interpretation was validated by site surveys. The accuracy of the
145 results was verified by establishing a confusion matrix. Random points were selected in the
146 Erdas Imagine 2015 software for classification, where a certain number of random points were
147 selected for each category. The classification of each random point was distinguished visually so

148 that the category to which each random point belongs is defined in the software. The user
 149 accuracy, producer accuracy, and Kappa coefficient of the overall classification of each category
 150 were then calculated.

151 **Vegetation coverage calculation**

152 Plant coverage information is typically extracted from remote sensing images. Given the high
 153 accuracy of NDVI values estimated using remote sensing, it is one of the most widely used
 154 indexes (Mu et al., 2012). A common method to calculate vegetation coverage is based on the
 155 hybrid pixel decomposition method, where it is assumed that each pixel of the remote sensing
 156 image is composed of soil and vegetation components. Thus, the information includes both a
 157 pure soil component and a pure vegetation component. In this case, we assumed that the NDVI
 158 value is a weighted average sum of the index values from both soil and vegetation information
 159 (Li, Fan, & Wang, 2010), which is given as follows:

$$160 \quad NDVI = f_v \times NDVI_{veg} + (1 - f_v) \times NDVI_{soil}, \quad (1)$$

161 Where NDVI is the vegetation index value of mixed pixels; $NDVI_{veg}$ is the vegetation index of
 162 pure vegetation pixels; $NDVI_{soil}$ is the vegetation index value of pure soil pixels; and f_v is the
 163 vegetation coverage. Thus, the formula for vegetation coverage (f_v) becomes:

$$164 \quad f_v = (NDVI - NDVI_{soil}) / (NDVI_{veg} - NDVI_{soil}), \quad (2)$$

165 In practice, the parameters can be selected in the following ways. (1) Take different $NDVI_{veg}$
 166 and $NDVI_{soil}$ values for different soil and vegetation types. (2) Use the maximum and minimum
 167 NDVIs of the study area, $NDVI_{veg} = NDVI_{max}$, $NDVI_{soil} = NDVI_{min}$. (3) Determine the NDVI
 168 value of the corresponding pixel based on measured data (Li et al., 2015). Under the influence of
 169 varying meteorological conditions, vegetation type and distribution, seasons, and other factors,
 170 both the $NDVI_{soil}$ and $NDVI_{veg}$ values for different images vary to some extent.

171 The maximum and minimum values of the given confidence interval are selected, and the
 172 confidence value is determined primarily from the image size and clarity. As a comparison, the
 173 maximum NDVI images of 2015 and 2019 were extracted. In the NDVI frequency accumulation
 174 table, the NDVI with a frequency of 5% was selected for $NDVI_{soil}$, and the NDVI with a
 175 frequency of 95% was selected for $NDVI_{veg}$. Finally, the vegetation coverage was obtained from
 176 Eq. (2).

177 **Land surface temperature inversion**

178 The LST inversion algorithms for single-infrared-band Landsat 8 OLI remote sensing data are
 179 based primary on the radioactive transfer equation (RTE), a universal single-channel algorithm,
 180 and a single-window algorithm (Ding & Xu, 2008). Therefore, the RTE was selected to invert
 181 the LSTs in this study.

182 **Calculation of specific surface emissivity**

183 Remote sensing images were firstly classified into three types: water bodies, towns and natural
 184 surfaces. The specific emissivity of water pixels is 0.995, where other surface emissivity
 185 estimates were based on the following formulas (Chi, Zeng, & Wang, 2016):

$$186 \quad \varepsilon_{\text{surface}} = 0.9625 + 0.0614f_v - 0.0461f_v^2, \quad (3)$$

$$187 \quad \varepsilon_{\text{building}} = 0.9589 + 0.086f_v - 0.0671f_v^2, \quad (4)$$

188 Where $\varepsilon_{\text{surface}}$ and $\varepsilon_{\text{building}}$ represent the specific emissivity of natural surface pixels and urban
 189 pixels, respectively.

190 **Radioactive transfer equation**

191 The RTE is also called the atmospheric correction method. It firstly estimates the impact of the
 192 atmosphere on the surface thermal radiation based on the information received by the satellite
 193 thermal infrared sensor. This is then subtracted from the total thermal radiation obtained by the
 194 sensor. The impact of the atmosphere on the surface can be used to obtain the intensity of surface
 195 thermal radiation. Assuming that the surface and the atmosphere have Lambertian properties for
 196 thermal radiation, the corresponding LST can be obtained as (You, & Yan, 2009; Yue et al.,
 197 2019):

$$198 \quad L_\lambda = [\varepsilon \cdot B(T_S) + (1 - \varepsilon)L_\downarrow] \cdot \tau + L_\uparrow, \quad (5)$$

199 Where L_λ is the intensity of thermal radiation received by the satellite sensor, $\varepsilon(K)$ is the
 200 surface emissivity, T_S is the true LST, $B(T_S)$ ($\text{W m}^{-2} \text{sr}^{-1} \mu\text{m}^{-1}$) is the black body brightness
 201 corresponding to temperature T_S derived from Planck's law, τ is the transmittance of the
 202 atmosphere at thermal infrared wavelengths, L_\uparrow ($\text{W m}^{-2} \text{sr}^{-1} \mu\text{m}^{-1}$) is the atmospheric upward
 203 radiance, and L_\downarrow ($\text{W m}^{-2} \text{sr}^{-1} \mu\text{m}^{-1}$) is the atmospheric downward radiance. Based on the RTE,
 204 the $B(T_S)$ can be obtained as (Wu et al., 2016; Hou, & Zhang, 2019):

$$205 \quad B(T_S) = [L_\lambda - L_\uparrow - \tau \cdot (1 - \varepsilon)L_\downarrow] / \tau \cdot \varepsilon, \quad (6)$$

206 Where τ , L_\uparrow ($\text{W m}^{-2} \text{sr}^{-1} \mu\text{m}^{-1}$) and L_\downarrow ($\text{W m}^{-2} \text{sr}^{-1} \mu\text{m}^{-1}$) were determined from the official
 207 NASA website (<http://atmcorr.gsfc.nasa.gov/>) by inputting the imaging time, latitude and
 208 longitude, air pressure and other relevant information to the study area. After estimating the of
 209 black body radiance $B(T_S)$, which is the same as the real temperature on the ground, the inverse
 210 function of Planck's law gives the real temperature on the ground as (Chen, 2014) :

$$211 \quad T_S = K_2 / \ln \left(\frac{K_1}{B(T_S)} + 1 \right), \quad (7)$$

212 Where K_1 and K_2 are constants obtained by querying the Landsat metadata file. In this case,
 213 $K_1=774.8853$ and $K_2=1321.0789$ for Landsat 8 TIRS band 10.

214 **Normalized temperature index and temperature classification**

215 The ecological environment of coal mining areas is damaged to varying degrees, this changes
216 their LSTs and causes a series of significant ecological effects and environmental problems, such
217 as vegetation degradation and soil erosion (Dutta & Agrawal, 2003; Zhou & Zhang, 2005). We
218 used the urban heat island effect to explore the impact of coal mining activities on LSTs (Ye et
219 al., 2011; Li et al., 2019). The formula for the normalized temperature index is:

$$220 \quad T_r = \frac{\Delta T}{T_{range}} = \frac{T - T_{min}}{T_{max} - T_{min}}, \quad (8)$$

221 Where T_r is the normalized temperature index, T is the temperature at any spatial position in
222 the region, T_{max} and T_{min} are the highest and lowest temperature in the region, respectively.

223 The method of equal intervals is used to divide the temperature based on the site conditions
224 and existing research (Sheng et al., 2010; Jia & Liu, 2006). Once the maximum and minimum
225 values of the inversion temperature are taken as endpoints, the temperature is divided into five
226 equal-spaced intervals. These are a low-temperature zone, a low-middle-temperature zone, a
227 middle-temperature zone, a middle-high-temperature zone, and a high-temperature zone. The
228 normalized temperature indices for these levels were 0.0–0.2, 0.2–0.4, 0.4–0.6, 0.6–0.8, and 0.8–
229 1.0, respectively (Table 1). Analyzing changes in the LST index at different distances from the
230 mine allows evaluating the intensity and range of the heat island effect as caused by coal-mining
231 activities.

232 **Analytical method of factors affecting land surface temperature**

233 The terrain over the study area is relatively flat, which facilitates farming, town construction, and
234 coal mining activities. We analyzed the spatial differentiation of LSTs in this area, which was
235 linked to land use, vegetation coverage and coal mining activities.

236 **The influence of land-use classification on land surface temperature**

237 The area and proportion of different types of land use were counted separately. Subsequently, the
238 land-use and the LST maps were superimposed to obtain statistical data on the LSTs of various
239 land-use types.

240 **The influence of vegetation coverage on land surface temperature**

241 A profile analysis more intuitively reflected the relationship between changes in LST and
242 vegetation coverage at a given geographical location. Using the interpolation line function in
243 ArcGIS 10.5 to view profile values of LST and vegetation coverage from 2015 and 2019 to
244 compare and analyze their associated changes along profiles to evaluate the relationships
245 between these variables.

246 **The influence of coal mining activities on land surface temperature**

247 *The influence of patch area*

248 Firstly, all mining areas within a distance of 1500 m from the edge of the study area were
249 screened. These selected mining area patches were then counted and grouped based on area. We
250 then combined these data with our LST inversion to determine the maximum, minimum, and
251 average LSTs for different patches. Finally, the influence of these mining land patches on the
252 LSTs were evaluated.

253 *The influence of buffer range*

254 Buffers with a range of 100–1500 m at intervals of 100 m were set for each of the patches. The
255 average LST in each buffer zone was extracted, and the trends in the LSTs at varying distances
256 from the mining area were analyzed.

257

258 **Results**

259 **Land surface temperature inversion**

260 The LST results for the Jiguan, Didao and Chengzihe Districts of Jixi in 2015 and 2019 are
261 shown in Fig. 2 and Table 2. The temperatures in 2015 were in general higher than those in 2019.
262 The average LST over the entire study area was 25.64 °C in 2015 and 22.10 °C in 2019. There is
263 a similarity in the spatial distribution patterns of their LSTs. High temperatures are concentrated
264 in the south-central and southeast parts of the study area, while the temperatures in the west and
265 north are relatively low. In these two years, the average LST in the Jiguan District was higher
266 than averages in the other two districts, but its highest temperature was lower than the maximum
267 recorded in the Didao and Chengzihe Districts. The highest temperatures over the entire study
268 area were 42.29 °C, which was recorded at Shenghe Coal Mine in the Didao District. Likewise,
269 the highest temperature in the Chengzihe District was recorded at Chengshan Coal Mine. Thus,
270 mining areas had much higher LSTs than average. While only two years were selected for the
271 analysis, similar results validate the conclusions.

272 The LSTs from 2015 and 2019 were normalized and divided into five levels, as shown in Fig.
273 3 and Table 3. The LSTs in the study area were assigned primarily to the low-temperature, low-
274 middle-temperature, and middle-temperature zones, which covered the LST range of 19.16–
275 33.04 °C in 2015 and 16.29–29.37 °C in 2019. Among them, the low-middle-temperature zone
276 had the largest area as it accounted for more than 70% of the total study area. The high-
277 temperature and middle-high-temperature zones had smaller areas. The high-temperature zone
278 was distributed primarily within the Didao and Chengzihe Districts. The Shenghe Coal Mine
279 accounted for 53.08% of the total area of the high-temperature zone in 2015 and rose to 59.04%
280 in 2019. The proportion of the Chengshan Coal Mine in the total area of the high-temperature
281 zone increased from 8.17% to 34.47% over these four years. Meanwhile, the low-temperature
282 and low-middle-temperature zones were distributed mostly in the Didao and Chengzihe Districts,
283 giving a large temperature difference between them. Therefore, local heat island effects were
284 obvious within the study area.

285

286 **Land-use classification**

287 Land-use types in the Jiguan, Didao, and Chengzihe Districts of Jixi in 2015 and 2019 are shown
288 in Fig. 4 and Table 4. From 2015 to 2019, the area of forest land increased while the area of
289 cultivated land decreased. However, the dominant land-use types in the study area are still forest
290 land and cultivated land. The forest land is distributed mostly in the northern part of the study
291 area, while the cultivated land is distributed in the middle and southern parts. Construction land
292 is concentrated in the Jiguan District, which increased significantly from 109.94 km² to 133.69
293 km² in the four considered years. The mining land is defined primarily by the Shenghe Coal
294 Mine in the Didao District and the Chengshan Coal Mine in the Chengzihe District. The
295 accuracy of the land-use classification was verified by establishing a confusion matrix. The
296 matrix showed that the Kappa coefficients of the land-use maps in the interpreted periods are all
297 above 0.8, which meets the accuracy requirements for this study (Table 5).

298

299 **Vegetation coverage**

300 The remote sensing images of the study area were processed according to the mixed pixel
301 decomposition method to obtain the vegetation coverage of the Jiguan, Didao, and Chengzihe
302 District of Jixi (Fig. 5). The construction land in the eastern Jiguan District, Shenghe Coal Mine
303 in the Didao District and Chengshan Coal Mine in the Chengzihe District had the lowest
304 vegetation coverage. However, ongoing urbanization and coal mining activities have markedly
305 affected vegetation coverage in many other areas as well.

306

307 **Correlation between land surface temperature and land-use types**

308 The main land types in the low-temperature and low-middle-temperature zone are water areas,
309 forest land, grassland and cultivated land. The main land types in the high-temperature, middle-
310 high-temperature, and middle-temperature zones are construction land and mining land. There
311 are large difference in the average LSTs among these land-use types (Table 6). The average
312 LSTs for mining land, construction land and grassland were higher than the average LST for the
313 study area. Among them, mining land had the highest average LSTs (33.33 °C in 2015 and 29.63
314 °C in 2019), yielding temperature anomalies of 7.69 °C in 2015 and 7.53 °C in 2019. The water
315 area had the lowest average LSTs (21.72 °C in 2015 and 19.31 °C in 2019). At the same time, the
316 temperature standard deviation within the mining land was also relatively large, with a difference
317 of 18.02 °C between the minimum and maximum temperatures.

318

319 **Correlation between land surface temperature and vegetation coverage**

320 An east–west transect was drawn across the study are, and the data from 2019 were used to
321 analyze changes in the LSTs with vegetation coverage. Every 25 pixel points on the profile were
322 assigned to a group, and the average value of the vegetation coverage and LST in each group was
323 calculated to obtain 56 data sets. Finally, a linear fit was performed between the vegetation
324 coverage and average LST, and the coefficient of determination was assessed (Fig. 6). Areas
325 with low vegetation coverage were associated with higher LSTs. In addition, as vegetation
326 coverage decreased, the LSTs increased. The trends in LST and vegetation coverage were
327 opposite with reciprocal change patterns.

328 The linear fit of the average LST and vegetation coverage (Fig. 7) shows that if the vegetation
329 coverage increases by 0.1, the average LST is expected to decrease by approximately 0.75 °C.
330 This constitutes a strong negative relationship between the LST and vegetation coverage. Using
331 the SPSS 24 (IBM, Corp., Armonk, NY, USA) indicated a correlation coefficient of $R = -0.780$.
332 This indicates a significant correlation at the 0.01 confidence level (both sides). Thus, green
333 vegetation has a significant cooling effect on the land surface.

334

335 **Correlation between land surface temperature and coal mining activities**

336 This study mainly considers spatial variations when exploring the correlation between the LST
337 and mining activities. Therefore, the data of the most recent year (2019) is selected for the
338 analysis, and the spatial distribution of the LST is analyzed based on the patch area and buffer
339 sizes.

340 **Correlation between land surface temperature and patch area of mining lands**

341 The mining areas were grouped based on patch area after screening them within 1500 m of the
342 edge of the study area. The maximum, minimum and average LSTs of each patch were
343 calculated from the 52 data sets (Table 7). Correlations among the average patch area and the
344 average and maximum patch temperatures were analyzed using SPSS 24. Our analysis indicates
345 that the patch was strongly positively correlated with the average and maximum patch
346 temperatures.

347 Correlation between the patch area and average patch temperature (Fig. 8) yielded $R = 0.571$.
348 This indicates a significant correlation at the 0.01 confidence level (both sides). The
349 determination coefficient of the fit logarithmic function was $R^2 = 0.487$, indicating that larger
350 patch sizes promote a greater average patch temperature. Within 200,000 m², the average patch
351 temperature increases rapidly with the size of the patch area. Once above 200,000 m², the
352 average patch temperature increases more slowly.

353 The correlation between the patch area and maximum patch temperature (Fig. 9) yielded $R =$
354 0.645. This indicates a significant correlation at the 0.01 confidence level (both sides). The
355 determination coefficient of the linear fit was $R^2 = 0.415$, indicating that larger patch sizes

356 promote a greater maximum patch temperature. If the patch area of mining land increases by
357 100,000 m², the maximum patch temperature will increase by approximately 0.81°C.

358 **Correlation between land surface temperature and various buffer sizes**

359 The schematic diagram of buffer zone in mining land patch is shown in Fig 10. A correlation
360 analysis was performed on average patch area, average patch temperature, maximum patch
361 temperature of mining land and the average LST in buffer zones at 100–1500 m reviewed at
362 100m intervals (Table 8). The temperature of the buffer zones within 0–100 m was strongly
363 correlated with the patch area, average patch temperature, and maximum patch temperature of
364 the mining land. In the 100–200 m buffer zone, the correlation between the temperature and the
365 average area was not significant. Therefore, a higher correlation was found for the entire buffer
366 zone with the average and maximum patch temperatures, while a lower correlation was found
367 with the patch area. Thus, the correlation between the temperature in the buffer zone and the
368 average patch temperature was most relevant.

369 To further study the correspondence between the average patch temperature of mining land
370 and the temperature in the buffer zones, the 52 data sets were sorted based on their average patch
371 temperatures from smallest to largest. Each of the 13 groups was then compiled into a new
372 group. The average number and the average temperature of the corresponding buffer zone in
373 each new group were calculated to obtain four new data sets (Table 9).

374 Figure 11 shows that the further the buffer zone was from the mine land patch, the lower its
375 temperature. In 0–200 m buffer zones, the average temperature changed drastically, while the
376 average temperature outside the 200 m zone varied little. The range of this heating effect is
377 approximately 700 m in Group 1, 1200 m in Group 2 and 3, and more than 1400 m in Group 4.
378 Therefore, a larger average patch temperature in the mining land causes a higher temperature in
379 its buffer zone, and the greater the scope of its influence.

380

381 **Discussion**

382 **Impact of coal mining activities on surface temperatures**

383 As the largest coal city in Heilongjiang Province, Jixi has always utilized coal as its leading
384 industry. The main types of coal mining wasteland in Jixi City include mining subsidence, land
385 occupation, polluted wasteland, and excavated land, which account for 0.48%, 82.0%, 6.82%,
386 and 10.71% of the total coal mining wasteland, respectively (Di, Guan & Zheng, 2015). Coal
387 mining activities generate a significant amount of heat. Thus, regional heating within the city has
388 intensified when coupled with their high-energy consumption and high-heat producing
389 enterprises (Hu, Zhao & Dong, 2010). The ongoing economic development of mining areas has
390 increased both the population density and heat production from urban infrastructure.

391 The correlation between LST and coal mining activities has resulted in larger mining lands
392 with higher average and maximum patch temperatures. The available literature has shown that
393 the size, shape, number, and boundary properties of these patches affect their energy
394 transmissions. According to landscape ecological theory, the size and shape of these patches also
395 affect their energy accumulation. Likewise, some researchers have recognized that larger patches
396 of construction land have higher degrees of aggregation, more regular shapes, higher LSTs, and
397 more significant heat island effects (Yu, 2006; Fu, 2001; Xie, Wang & Fu, 2011; Xu et al., 2015).
398 Some studies have analyzed different types of disturbances at the interior of mining lands,
399 among which dumps, opencast coal pits, and industrial centers have higher contributions to local
400 warming (Xie et al., 2011; Liu J, 2016). Exposed coal and coal gangue easily absorb heat and
401 cause increased temperatures, while piled coal gangue hills are prone to heat and spontaneous
402 combustion (Hao, 2011). Therefore, many factors cause high temperatures in mining land.

403 Quantitative research on the impact of mining land indicates a strong warming effect within a
404 buffer zone of 0–200 m around mining land patches. As the distance from the mining land
405 increases, the warming effects gradually weakens. Mining land patches with higher average
406 patch temperatures have larger temperature-affected buffer zones. Changes in the local
407 meteorological conditions, such as temperature rise, affect local species, which impacts the
408 ecological conditions of the entire region. However, the strength of the warming effect and the
409 size of its influence range are not only related to the distance from the mining land patch but may
410 also be related to the average temperature of the entire area during the analysis (Liao, 2009). This
411 specific correlation requires further study.

412 To date, regulations on the ecological and environmental protection are aimed only at the
413 ecological and environmental indicators within the mining area, which cannot achieve regional
414 ecological protection. Although it seems intuitive that coal production enterprises or units
415 engaged in corresponding activities have taken the responsibility of protecting the ecology and
416 environment, this does not cover the entire affected area of coal mining production activities. To
417 protect the ecological quality of the area while developing coal resources, the scope of
418 environmental protection in mining areas should be defined more scientifically and rationally.

419

420 **Impact of different land-use types on surface temperature**

421 Our results show that land-use types have a dominating impact on the LST. The LSTs of the
422 Jiguan, Didao, and Chengzihe District of Jixi were primarily within the range of 16.29–42.29 °C
423 in the two considered years. The low-middle-temperature zone had the largest area, which
424 accounted for 70.53% and 72.21% of the total area. The low-temperature zone was distributed
425 primarily over water areas, forest lands and cultivated lands. The high-temperature zone was
426 distributed mostly over the construction land and mining land, especially the Shenghe Coal Mine
427 in the Didao District and the Chengshan Coal Mine in the Chengzihe District.

428 The temperatures in 2019 were generally lower than those in 2015. From a normalized
429 comparison, it is seen that the high-temperature and low-temperature zones increased in 2019.
430 Along with the clustered development of mining land patches, the land surface temperature
431 shows a polarizing trend. The expansion of some high-temperature zones may be due to the
432 continued development of coal mines. The increased low-temperature areas may be due to the
433 reclamation and restoration of vegetation in mining areas. Based on governmental planning
434 (“Mineral Resources Planning of Jixi City (2016–2020)” and “Special Planning for Reclamation
435 and Utilization of Desert Land of Industrial Mining Area and Mining Subsidence Area in Jixi
436 City (2014–2020)”) from 2015 to 2019, the coal industry wastelands in Chengzihe and Didao
437 Districts were treated to a certain extent, and the reclaimed land was converted into cultivated
438 land, forest land, and construction land. These lands will be used for agricultural production,
439 creating recreational landscapes, and improving the ecological environment.

440 In recent years, the development of coal resources in Jixi has been rapid. Additionally, the
441 spatial distribution of mines has also changed (Yang, 2013). Construction and mining activities
442 have reduced the “cooling” land-use types, such as forest and cultivated lands (Wang et al.,
443 2020), and replaced them with “warming” types, like construction and mining lands. The
444 available literature has shown that urban expansion is the main driving process of land cover
445 changes and consequently rise of LST (Pal & Ziaul, 2017), which is consistent with our findings.
446 With changes in land-use types, natural vegetation has been replaced by impervious concrete and
447 construction land, which has caused significant changes like heat radiation from the underlying
448 city surface (Wang et al., 2013). These man-made surfaces have a strong light absorptive effect
449 and can quickly raise the local LST (Hien et al., 2011). In addition, building facades can reflect
450 light multiple times, heating the near-surface atmosphere and cause LSTs to rise significantly
451 (Miao et al., 2009). Some studies have also shown that the heating effect of construction lands,
452 especially compact low-rise buildings, is very obvious (Das, Das & Mandal, 2020). Among the
453 six considered land-use types, the LSTs of water area, forest land, and cultivated land were lower
454 than the average LST for the study area. Water-permeable areas of the study region, such as
455 water areas and forest land, ensure efficient heat exchange between the soil and the atmosphere.
456 Water can evaporate, which absorbs heat in the environment and has an overall cooling effect
457 (Zhang et al., 2013). Therefore, not only by balancing the land-use types, but also by optimizing
458 appropriate urban planning, the increase in LST can be adjusted to reduce the impact of
459 urbanization on the ecological environment (Das & Das, 2020).

460

461 **Impact of vegetation coverage on land surface temperatures**

462 Our coupling analysis showed that changes in vegetation coverage are very important factors that
463 affecting ecological status change. There is a significant negative correlation between LST and
464 vegetation coverage, which has also been confirmed by other works (Estoque, Murayama &
465 Myint, 2017; Jiang, Zeng & Zeng, 2015; Duan & Zhang, 2012; Wu, Xu & Tan, 2007; Yue, Xu &

466 Xu, 2006). As vegetation blocks sunlight, it reduces the amount of solar radiation that reaches
467 the surface, while plant transpiration also reduces the LST (Cui, Li & Ji, 2018). In areas with
468 high vegetation coverage, the LST was lower than in other areas, illustrating the degree to which
469 vegetation could effectively alleviate heat island effect.

470 Therefore, municipal bodies should carefully consider the balance between ecological
471 protection and economic development. The focus should be on vegetation restoration and
472 environmental governance in areas where heat emissions are concentrated, such as abandoned
473 mine sites and barren areas. Meanwhile, increasing the proportion of green space, improving the
474 diversity and complexity of the landscape, and dividing the impervious surface with vegetation
475 when developing urban construction land and coal mines can significantly reduce the LST and
476 alleviate heat island effects.

477

478 **Conclusions**

479 Our findings show that coal mining activities and urban expansion are the primary factors
480 affecting LSTs. These two factors change land-use types and vegetation coverage, which results
481 in an abnormal heat flux. There were large differences in the LSTs among the various land-use
482 types in Jixi City. The LSTs for the considered land-use types were ranked from high to low, as
483 follows: mining land > construction land > grassland > cultivated land > forest land > water area.
484 The average LST difference between the mining land and water area was more than 10 °C each
485 year.

486 Correlations between LST and vegetation coverage indicate that they have a significant
487 negative relationship. The LST was lower in areas with higher vegetation coverage than in other
488 areas. For every 0.1 increase in vegetation coverage, the surface temperature is expected to drop
489 by approximately 0.75 °C, indicating the extent to which vegetation can effectively alleviate
490 warming effects.

491 The correlation between the LST and coal mining activities indicates the patch area of the
492 mining land has a significant positive correlation with both the average and maximum patch
493 temperatures. The average patch temperature shows a logarithmic increase with the growth of the
494 patch area; thus, the average patch temperature increases significantly within 200,000 m². The
495 maximum patch temperature shows a linear increase with the growth of the patch area; thus, the
496 maximum patch temperature increases by approximately 0.81 °C for every 100,000 m² increase
497 in the patch area of mining land. A higher correlation was found between the average patch
498 temperature and the temperature in the buffer zone. This study found that the higher the average
499 patch temperature of mining land, the higher the temperature in its buffer zone, and the greater
500 the scope of its influence. As the distance from the mining land increased, its heating effect
501 weakened.

502 Full consideration should be given to vegetation restoration in mining areas to reduce the
503 warming effect from coal mining activities, especially in abandoned mining land, by increasing
504 the total vegetation coverage in the study area. The existing large coal mine land patches need to
505 be divided by plants or water areas. Thus, the scope of environmental protection in mining areas
506 needs to be correctly defined. Meanwhile, in future urban layouts, downtown areas should
507 maintain a proper distance from coal mining land. This study provides a useful reference to
508 explore the warming effects caused by coal mining activities and the definition of its influence
509 scope.

510

511 Funding

512 This work was supported by the Fundamental Research Funds for the Central Universities
513 (No.2572017CA12, No.2572018CP06).

514

515

516 References

- 517 **Bian ZF, Lei SG, Jin D, Wang L. 2018.** Several basic scientific issues related to mined land
518 remediation. *Journal of China Coal Society* **43(01)**:190-197
519 DOI 10.13225/j.cnki.jccs.2017.4004
- 520 **Chabukdhara M, Singh OP. 2016.** Coal mining in northeast India: an overview of
521 environmental issues and treatment approaches. *International Journal of Coal Science &*
522 *Technology* **3(2)**:87-96 DOI 10.1007/s40789-016-0126-1
- 523 **Chen Y. 2014.** A preliminary study on the urban heat island effect based on Landsat 8: case of
524 Xiamen City. *Geomatics & Spatial Information Technology* **37(02)**:123-128
525 DOI 10.3969/j.issn.1672-5867.2014.02.036
- 526 **Chi TL, Zeng J, Wang ST. 2016.** Research of the relationship between vegetation fraction and
527 evolution of thermal environment in Zhengzhou based on RS and GIS technology. *Chinese*
528 *Landscape Architecture* **32(10)**:78-83
- 529 **Cui LL, Li GS, Ji DJ. 2018.** Heat island effect and its relationship with land use in Chengdu
530 City. *Chinese Journal of Ecology* **37(05)**:1518-1526
531 DOI 10.13292/j.1000-4890.201805.001
- 532 **Das M, Das A. 2020.** Assessing the relationship between local climatic zones (LCZs) and land
533 surface temperature (LST) - A case study of Sriniketan-Santiniketan Planning Area (SSPA),
534 West Bengal, India. *Urban Climate* **32**:100591 DOI 10.1016/j.uclim.2020.100591
- 535 **Das M, Das A, Mandal S. 2020.** Outdoor thermal comfort in different settings of a tropical
536 planning region: A study on Sriniketan-Santiniketan Planning Area (SSPA), Eastern India.
537 *Sustainable Cities and Society* **63**:102433 DOI 10.1016/j.scs.2020.102433

- 538 **Ding F, Xu HQ. 2008.** Comparison of three algorithms for retrieving land surface temperature
539 from Landsat TM thermal infrared band. *Journal of Fujian Normal University (Natural*
540 *Science Edition)* **99(01)**:91-96
- 541 **Duan JL, Zhang XL. 2012.** Correlative analysis of the diversity patterns of regional surface
542 water, NDVI and thermal environment. *Chinese Journal of Applied Ecology* **23(10)**:2812-
543 2820 DOI 10.13287/j.1001-9332.2012.0400
- 544 **Dutta RK, Agrawal M. 2003.** Restoration of opencast coal mine spoil by planting exotic tree
545 species: a case study in dry tropical region. *Ecological Engineering* **21(2-3)**:143-151
546 DOI 10.1016/j.ecoleng.2003.10.002
- 547 **Estoque RC, Murayama Y, Myint SW. 2017.** Effects of landscape composition and pattern on
548 land surface temperature: An urban heat island study in the megacities of Southeast Asia.
549 *Science of the Total Environment* **577**:349-359 DOI 10.1016/j.scitotenv.2016.10.195
- 550 **Fu BJ. 2001.** Principle and response of landscape ecology. Beijing: Science Press.
- 551 **He L. 2010.** Synthetic evaluation of ecological environment influence, ecological environmental
552 protection and ecology repair countermeasures for open-pit mining. D. Thesis, Northwest
553 University.
- 554 **Hou YC, Zhang DY. 2019.** Comparison study on land surface temperature retrieval algorithms
555 based on Landsat 8 remote sensing image **35(10)**:142-147
556 DOI 10.11924/j.issn.1000-6850.casb18120100
- 557 **Hien WN, Kardinal JS, Samsudin R, Eliza A, Ignatius M. 2011.** A climatic responsive urban
558 planning model for high density city: Singapore's commercial district. *International Journal*
559 *of Sustainable Building Technology and Urban Development* **2(4)**:323-330
- 560 **Hu WL, Zhao P, Dong ZY. 2010.** Thermal environment effect of coal mining area and its
561 ecological significance based on TM data. *Journal of Hefei University of Technology*
562 *(Natural Science)* **33(05)**:741-744
- 563 **Hu ZQ, Duo LH, Wang XT. 2018.** Principle and method of reclaiming subsidence land with
564 inter-layers of filling materials. *Journal of China Coal Society* **43(01)**:198-206
565 DOI 10.13225/j.cnki.jccs.2017.4003
- 566 **Jia HF, Liu XH. 2006.** Principle and application of environmental remote sensing. Beijing:
567 Tsinghua University Press.
- 568 **Jiang MZ, Zeng SP, Zeng J. 2015.** Urban expansion of Tianjin and the micro climate
569 characteristics evolution: based on the urban thermal environment perspective. *Journal of*
570 *Arid Land Resources and Environment* **29(09)**:159-164
571 DOI 10.13448/j.cnki.jalre.2015.310
- 572 **Li DK, Fan JZ, Wang J. 2010.** Change characteristics and their causes of fractional vegetation
573 coverage (FVC) in Shanxi Province. *Chinese Journal of Applied Ecology* **21(11)**:2896-2903
574 DOI 10.13287/j.1001-9332.2010.0404
- 575 **Li HZ, Chen JS, Han Y, Zhang YN. 2019.** Micro-scale research of the impact factors on urban
576 thermal environment: a case study of Luohu District, Shenzhen. *Ecology and*
577 *Environmental Sciences* **28(08)**:1622-1631

- 578 DOI 10.16258/j.cnki.1674-5906.2019.08.015
- 579 **Li RL, Shi YJ, Yao YM, Tian FP, Hu Y. 2014.** Temporal and spatial variation of oasis cold
580 island effect in Ganzhou district of Zhangye based on Landsat TM/ETM+. *Journal of Arid*
581 *Land Resources and Environment* **28(09)**:139-144 DOI 10.13448/j.cnki.jalre.2014.09.012
- 582 **Li ZL, Duan SB, Tang BH, Wu H, Ren HZ, Yan GJ, Tang RL, Leng P. 2016.** Review of
583 methods for land surface temperature derived from thermal infrared remotely sensed data.
584 *Journal of Remote Sensing* **20(05)**:899-920 DOI 10.11834/jrs.20166192
- 585 **Liang BP, Zhai LX. 2014.** A Research on spatial-temporal changes and correlation between
586 vegetation fraction and land surface temperature in Guilin during 1991—2006. *Chinese*
587 *Landscape Architecture* **30(07)**:77-81
- 588 **Liao CH. 2009.** Study on ecological effects of mining landscape and ecological restoration in
589 Yangquan coal mining region. M. Thesis, Tsinghua University.
- 590 **Liu JY, Kuang WH, Zhang ZX, Xu XL, Qin YW, Ning J, Zhou WC, Zhang SW, Li RD,**
591 **Yan CZ, Wu SX, Shi XZ, Jiang N, Yu DS, Pan XZ, Chi WF. 2014.** Spatiotemporal
592 characteristics, patterns and causes of land use changes in China since the late 1980s. *Acta*
593 *Geographica Sinica* **69(01)**:3-14 DOI 10.11821/dlxb201401001
- 594 **Ma W, Zhao ZM, Liu X, Yan DC. 2010.** A quantitative analysis of the relationship between
595 vegetation indices and land surface temperature based on remote sensing: a case study of
596 TM data for Beijing. *Remote Sensing for Land & Resources* **22(04)**:108-112
597 DOI 10.6046/gtzyyg.2010.04.22
- 598 **Marceau DJ, Howarth PJ, Dubois JM, Gratton DJ. 2003.** Evaluation of the grey-level co-
599 occurrence matrix method for land-cover classification using spot imagery. *IEEE*
600 *Transactions on Geoscience and Remote Sensing* **28(4)**:513-519
601 DOI 10.1109/TGRS.1990.572937
- 602 **Miao S, Chen F, Lemone MA, Tewari M, Wang Y. 2009.** An observational and modeling
603 study of characteristics of urban heat island and boundary layer structures in Beijing.
604 *Journal of Applied Meteorology and Climatology* **48(3)**:484-501
605 DOI 10.1175/2008JAMC1909.1
- 606 **Mooney HA, Duraiappah A, Larigauderie A. 2013.** Evolution of natural and social science
607 interactions in global change research programs. *Proceedings of the National Academy of*
608 *Sciences* **110**:3665-3672 DOI 10.1073/pnas.1107484110
- 609 **Mu SJ, Li JL, Chen YZ, Gang CC, Zhou W, Ju WM. 2012.** Spatial differences of variations
610 of vegetation coverage in inner Mongolia during 2001-2010. *Acta Geographica Sinica*
611 **67(09)**:1255-1268 DOI 10.11821/xb201209010
- 612 **Pal S, Ziaul S. 2017.** Detection of land use and land cover change and land surface temperature
613 in English Bazar urban centre. *The Egyptian Journal of Remote Sensing and Space Science*
614 **20(1)**:125-145 DOI 10.1016/j.ejrs.2016.11.003
- 615 **Pan DL, Huang ZQ, Zhang DR, Wang J, Zhou LF. 2013.** Mapping land subsidence related to
616 underground coal fires in the Wuda Coalfield (Northern China) using a small stack of
617 ALOS PALSAR differential interferograms. *Remote Sensing* **5(3)**:1152-1176

- 618 DOI 10.3390/rs5031152
- 619 **Wang RC, Hou H, Murayama Y, Derdouri A. 2020.** Spatiotemporal Analysis of Land
620 Use/Cover Patterns and Their Relationship with Land Surface Temperature in Nanjing,
621 China. *Remote Sensing* **12(3)**:440 DOI 10.3390/rs12030440
- 622 **Wang W, Shen SH, Zhao XY, Yang SB. 2011.** Comparative analysis on quantitative
623 relationships between NDVI, RSR and land surface temperature. *Resources and*
624 *Environment in the Yangtze Basin* **20(04)**:439-444
- 625 **Wu JW, Xu JH, Tan WQ. 2007.** Study on the relationship of urban heat island and vegetation
626 abundance in Shanghai City. *Remote Sensing Technology and Application* **22(01)**:26-30
627 DOI 10.11873/j.issn.1004-0323.2007.1.26
- 628 **Wu ZG, Jiang T, Fan YL, Chen LJ. 2016.** Land surface temperature retrieval and result
629 analysis based on Landsat 8 data in Wuhan City. *Chinese Journal of Engineering*
630 *Geophysics* **13(01)**:135-142 DOI 10.3969/j.issn.1672-7940.2016.01.023
- 631 **Xiao W, Hu ZQ, Fu YH. 2014.** Zoning of land reclamation in coal mining area and new
632 progresses for the past 10 years. *International Journal of Coal Science & Technology*
633 **1(2)**:177-183 DOI 10.1007/s40789-014-0024-3
- 634 **Xie MM, Wang YL, Fu MC. 2011.** An overview and perspective about causative factors of
635 surface urban heat island effects. *Progress in Geography* **30(01)**:35-41
636 DOI 10.11820/dlkxjz.2011.01.004
- 637 **Xu S, Li FX, Zhang LB, Zhou, L. 2015.** Spatiotemporal changes of thermal environment
638 landscape pattern in Changsha. *Acta Ecologica Sinica* **35(11)**:3743-3754
639 DOI 10.5846/stxb201310142477
- 640 **Xu HQ, He H, Huang SL. 2013.** Analysis of fractional vegetation cover change and its impact
641 on thermal environment in the Hetian basinal area of County Changting, Fujian Province,
642 China. *Acta Ecologica Sinica* **33(10)**:2954-2963 DOI 10.5846/stxb201205150720
- 643 **Yang JH. 2013.** Evaluation Research on Land Sustainable Use of Jixi City with Coal Resource-
644 exhausted. M. Thesis, Northeast Agricultural University.
- 645 **Ye CH, Liu YH, Liu WD, Liu C, Quan WJ. 2011.** Research on urban surface heat
646 environment monitoring indexes and its application. *Meteorological Science and*
647 *Technology* **39(01)**:95-101 DOI 10.19517/j.1671-6345.2011.01.019
- 648 **You X, Yan LM. 2009.** Retrieving land surface temperature from the ETM+ image radioactive
649 transfer equation. *Sci-Tech Information Development & Economy* **19(27)**:134-136+138
- 650 **Yu XX. 2006.** *Landscape Ecology*. Beijing: Higher Education Press.
- 651 **Yue TC, Nie S, Pan H, Li LC. 2019.** Land surface temperature retrieval and urban heat island
652 effect based on Landsat 8 image in Fuzhou City. *Journal of Northwest Forestry University*
653 **34(05)**:154-160 DOI 10.3969/j.issn.1001-7461.2019.05.24
- 654 **Yue WZ, Xu JH, Xu LH. 2006.** An analysis on eco-environmental effect of urban land use
655 based on remote sensing images: a case study of urban thermal environment and NDVI.
656 *Acta Ecologica Sinica* **26(05)**:1450-1460

- 657 **Zhang F, Tashpolat T, Ding JL, Mamat S, Nigala T, Gui DW, Wang JS. 2013.** The heat
658 environment of land surface of typical oasis in upper reaches of Tarim river with remote
659 sensing images. *Journal of Arid Land Resources and Environment* 27(04):111-116
660 DOI 10.13448/j.cnki.jalre.2013.04.014
- 661 **Zhang H, Qi ZF, Ye XY, Cai YB, Ma WC, Chen MN. 2013.** Analysis of land use/land cover
662 change, population shift, and their effects on spatiotemporal patterns of urban heat islands
663 in metropolitan Shanghai, China. *Applied Geography* 44:121-133
664 DOI 10.1016/i.apgeog.2013.07.021
- 665 **Zhou JH, Wang LJ. 2014.** Comprehensive study on ecological restoration and land exploitation
666 of mining subsidence in suburbs of Chinese mining cities. *International Journal of Coal*
667 *Science & Technology* 1(2):248-252 DOI:10.1007/s40789-014-0035-0
- 668 **Zhou QX, Zhang QR. 2005.** Environmental problems and ecological countermeasures of coal-
669 mining areas in the old industrial base, Northeastern China. *Chinese Journal of Ecology*
670 24(03):287-290 DOI 10.13292/j.1000-4890.2005.0254
- 671 **Zhu ZR, Cheng PG, Gui X, Teng Y, Tong CZ. 2016.** Overview of surface temperature
672 inversion algorithm. *Geomatics & Spatial Information Technology* 39(05):70-75
673 DOI 10.3969/j.issn.1672-5867.2016.05.020

Table 1 (on next page)

Table 1 The relationship between the normalized temperature index values and assigned temperature grades

1 **Table 1 The relationship between the normalized temperature index values and assigned**
2 **temperature grades**

Normalized temperature index	Temperature grade
0.0-0.2	Low temperature zone
0.2-0.4	Low-middle temperature zone
0.4-0.6	Middle temperature zone
0.6-0.8	Middle-high temperature zone
0.8-1.0	High temperature zone

3

4

Table 2 (on next page)

Table 2 Statistics on LST for the study area in 2015 and 2019

1

Table 2 Statistics on LST for the study area in 2015 and 2019

Range	Land surface temperature/°C							
	2015				2019			
	MEAN	MIN	MAX	STD	MEAN	MIN	MAX	STD
Jiguan District	27.16	21.58	38.97	2.52	23.24	17.42	33.64	2.23
Didao District	25.23	19.16	42.29	1.92	21.75	17.18	38.08	1.63
Chengzihe District	25.53	19.45	39.13	2.48	22.34	16.29	35.26	2.14
Total	25.64	19.16	42.29	2.28	22.10	16.29	38.08	1.95

2

Table 3 (on next page)

Table 3 LST normalization results for the study area in 2015 and 2019

1 **Table 3 LST normalization results for the study area in 2015 and 2019**

Temperature grade	Normalized temperature index	2015		2019	
		LST / °C	Percentage	LST / °C	Percentage
Low temperature zone	0.0-0.2	19.16-23.78	18.19%	16.29-20.65	19.31%
Low-middle temperature zone	0.2-0.4	23.78-28.41	70.53%	20.65-25.01	72.21%
Middle temperature zone	0.4-0.6	28.41-33.04	10.34%	25.01-29.37	7.79%
Middle-high temperature zone	0.6-0.8	33.04-37.66	0.90%	29.37-33.72	0.66%
High temperature zone	0.8-1.0	37.66-42.29	0.04%	33.72-38.08	0.03%
Total	0.0-1.0	19.16-42.29	100.00%	16.29-38.08	100.00%

2

3

Table 4 (on next page)

Table 4 Land-use structure for the study area in 2015 and 2019

1

Table 4 Land-use structure for the study area in 2015 and 2019

Land-use	2015		2019	
	Area / km²	Percentage / %	Area / km²	Percentage / %
Forest land	294.07	35.52%	304.18	36.74%
Grassland	52.95	6.39%	80.4	9.71%
Construction land	109.94	13.28%	133.69	16.15%
Cultivated land	357.39	43.17%	295.07	35.64%
Mining land	7.10	0.86%	6.76	0.82%
Water area	6.42	0.78%	7.77	0.94%
Total	827.87	100.00%	827.87	100.00%

2

3

Table 5 (on next page)

Table 5 Accuracy evaluation of land use classification for the study area in 2015 and 2019

1 **Table 5 Accuracy evaluation of land use classification for the study area in 2015 and 2019**

2015							
Land-use	Forest	Grassland	Construction	Cultivated	Mining	Water	Total
	land		land	land	land	area	
Forest land	1646	2	–	–	–	–	1648
Grassland	–	150	–	–	–	–	150
Construction land	3	–	2406	–	–	–	2409
Cultivated land	–	4	2	1737	–	–	1743
Mining land	–	–	17	–	346	–	363
Water area	–	–	–	–	–	319	319
Total	1649	156	2425	1737	346	319	6632
Producers Accuracy	99.82	96.15	99.22	1000	100	98.46	–
Users Accuracy	99.88	100	99.67	99.66	95.32	100	–
2019							
Land-use	Forest	Grassland	Construction	Cultivated	Mining	Water	Total
	land		land	land	land	area	
Forest land	858	35	–	–	–	–	893
Grassland	–	37	34	10	1	–	82
Construction land	–	–	1710	35	18	–	1763
Cultivated land	2	11	19	821	2	–	855
Mining land	–	–	2	–	263	–	265
Water area	–	–	–	–	–	231	231

Total	860	83	1765	866	284	231	4089
Producers Accuracy	99.77	44.58	96.88	94.8	92.61	92.4	–
Users Accuracy	96.08	45.12	96.07	95.8	99.25	100	–

2 Note: In 2015, Overall Classification Accuracy=99.50%; Overall Kappa Statistics=0.9932;

3 In 2019, Overall Classification Accuracy=95.42%; Overall Kappa Statistics=0.9361.

4

Table 6 (on next page)

Table 6 Statistics on LST of different land-use types in 2015 and 2019

1

Table 6 Statistics on LST of different land-use types in 2015 and 2019

Land use types	Land surface temperature/°C							
	2015				2019			
	MEAN	MIN	MAX	STD	MEAN	MIN	MAX	STD
Forest land	23.95	20.79	30.89	1.01	21.07	17.38	26.41	0.97
Grassland	26.55	21.94	36.27	1.45	23.21	18.77	30.56	1.43
Construction land	29.12	20.59	41.74	2.26	24.62	17.24	35.04	1.96
Cultivated land	25.74	21.35	33.71	1.20	21.73	18.26	29.14	1.09
Mining land	33.33	24.27	42.29	2.50	29.63	20.35	38.08	2.31
Water area	21.72	19.16	29.12	2.30	19.31	16.29	27.56	1.74

2

3

Table 7 (on next page)

Table 7 Statistics on LST and patch area for mining lands

1

Table 7 Statistics on LST and patch area for mining lands

Average area			LST/°C			Average area			LST/°C		
/m ²			MEAN MAX			/m ²			MEAN MAX		
900	26.88	30.98	18000	29.09	30.27	53100	30.22	31.95			
1800	27.38	32.30	19800	29.17	35.11	58500	27.85	29.48			
2700	27.25	30.87	20700	31.85	33.43	61200	29.79	31.73			
3600	26.50	30.49	21600	29.60	30.61	65700	31.90	34.51			
4500	27.97	31.39	23400	29.29	30.25	82800	30.79	32.06			
5400	28.23	30.16	24300	28.47	31.40	88200	29.63	31.78			
6300	27.46	31.61	25200	29.02	30.51	110700	28.62	30.18			
7200	27.26	30.87	26100	27.89	29.30	114300	31.36	33.22			
8100	26.52	29.54	27000	28.26	29.43	135000	28.94	31.05			
9000	27.57	29.63	28800	28.59	31.25	139500	28.70	31.22			
9900	28.39	30.63	31500	27.54	30.19	162000	29.85	32.49			
10800	28.23	31.98	32400	28.33	31.92	175500	30.14	32.31			
12600	28.26	33.02	36000	28.48	30.26	179100	30.13	32.35			
13500	29.44	30.58	39600	28.54	30.53	241200	29.04	31.41			
14400	26.99	29.11	40500	27.86	30.36	490500	31.15	33.10			
15300	25.58	26.63	43200	28.33	30.66	626400	31.58	35.26			
16200	27.53	28.46	48600	29.85	31.84	754200	31.58	38.08			
17100	26.57	29.39									

2

Table 8 (on next page)

Table 8 Correlation between LST and buffer zone within the mining lands

1 **Table 8 Correlation between LST and buffer zone within the mining lands**

Factor	Average	Average	Maximum
	Area	Temperature	Temperature
100m	0.35**	0.79**	0.71**
200m	0.07	0.41**	0.39**
300m	-0.01	0.31*	0.26
400m	-0.03	0.30*	0.25
500m	0.01	0.33*	0.30*
600m	0.02	0.33*	0.28*
700m	0.03	0.30*	0.27
800m	0.05	0.28*	0.28*
900m	0.09	0.28*	0.30*
1000m	0.09	0.29*	0.29*
1100m	0.09	0.29*	0.28*
1200m	0.12	0.33*	0.30*
1300m	0.10	0.32*	0.27
1400m	0.08	0.29*	0.24
1500m	0.10	0.28*	0.26

2 Note: * means $p < 0.05$, ** means $p < 0.01$

3

Table 9 (on next page)

Table 9 Correspondence between LST and buffer zone within the mining lands

1 **Table 9 Correspondence between LST and buffer zone within the mining lands**

Average Temperature/°C	27.00	28.20	29.05	30.78
100m	25.15	25.84	26.01	27.17
200m	24.39	24.75	24.43	25.36
300m	24.34	24.65	24.16	25.11
400m	24.22	24.64	24.07	25.00
500m	24.06	24.69	24.04	24.97
600m	23.87	24.63	24.12	24.78
700m	23.76	24.53	24.14	24.59
800m	23.70	24.44	23.95	24.52
900m	23.64	24.24	23.80	24.47
1000m	23.59	24.06	23.77	24.41
1100m	23.54	23.87	23.72	24.29
1200m	23.48	23.68	23.71	24.21
1300m	23.43	23.57	23.68	24.07
1400m	23.43	23.55	23.66	23.96
1500m	23.42	23.52	23.51	23.92

2

Figure 1

Figure 1 Location map showing the three districts of Jixi comprising the study area

Map representing the geostrategic importance of the study area: (A) Jixi City, Heilongjiang Province, China, (B) Three districts of Jixi.

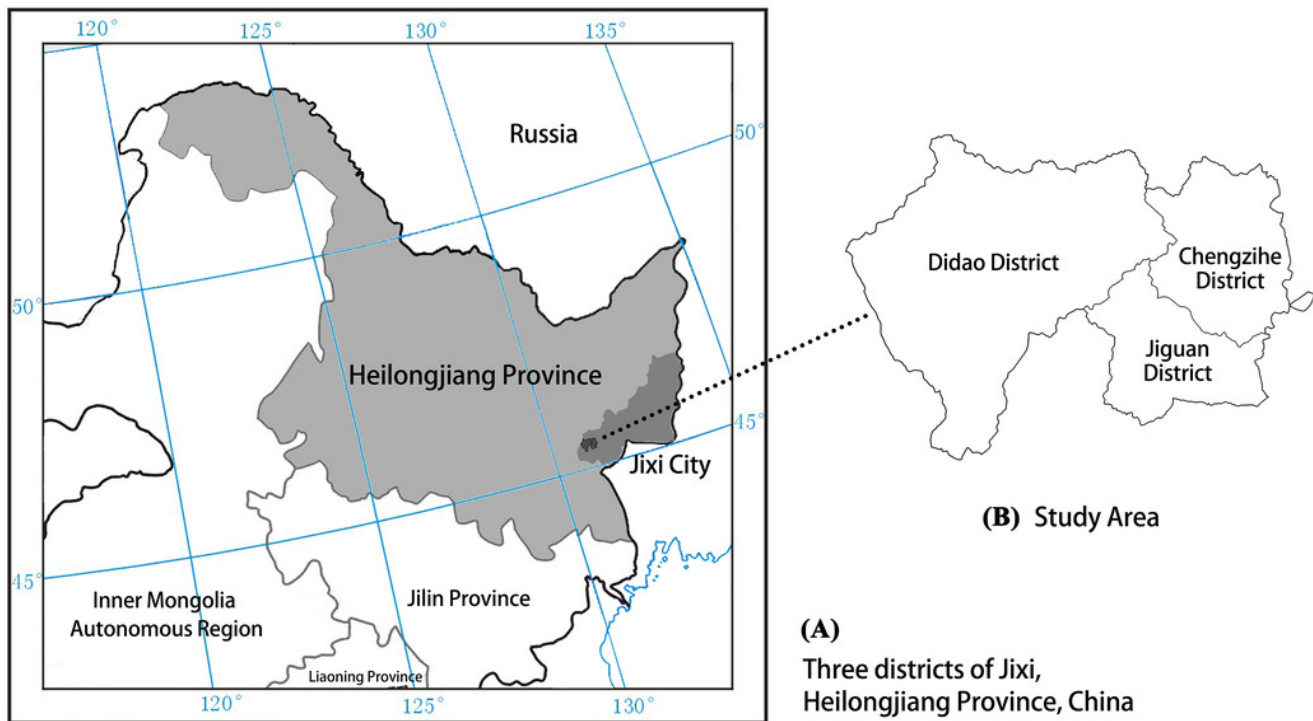


Figure 2

Land surface temperature ($^{\circ}\text{C}$) results for the three districts of Jixi in 2019

Land surface temperature (LST) maps for (A) 2015, (B) 2019 of the three districts in Jixi, Heilongjiang, China.

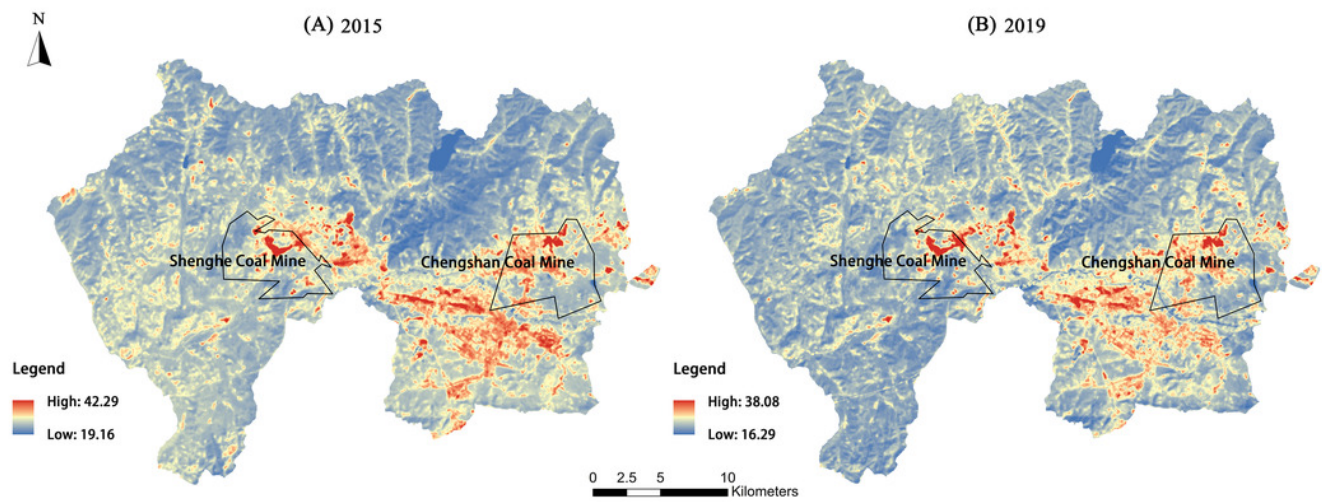


Figure 3

Figure 3 Spatial distribution of land surface temperature levels of the study area in 2015 and 2019

Spatial distribution of land surface temperature levels for (A) 2015, (B) 2019 of the three districts in Jixi, Heilongjiang, China.

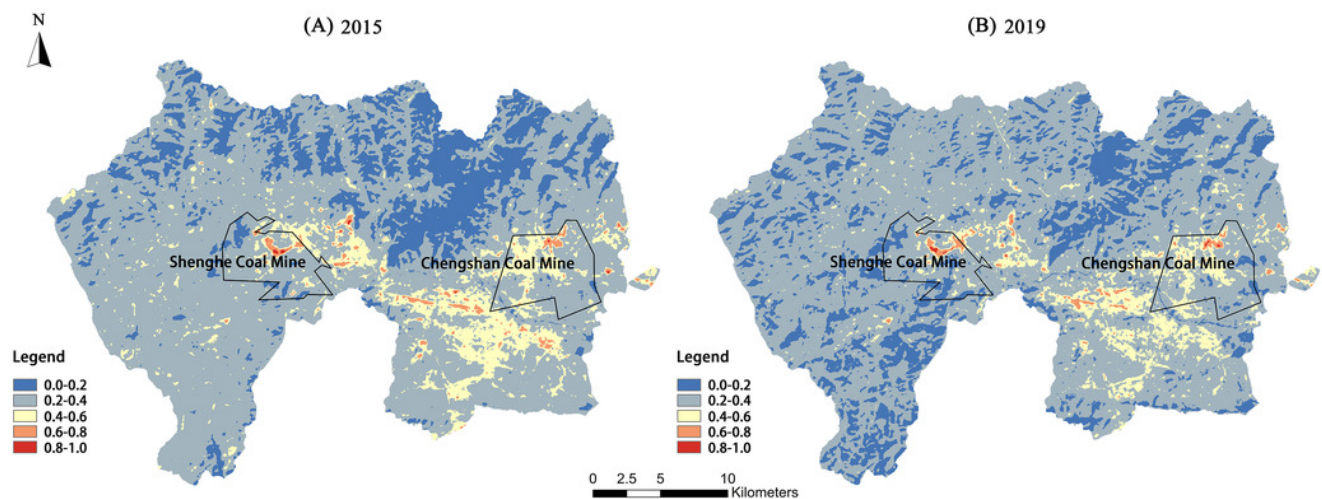


Figure 4

Figure 4 Land-use types of the study area in 2015 and 2019

Land-use types for (A) 2015, (B) 2019 of the three districts in Jixi, Heilongjiang, China.

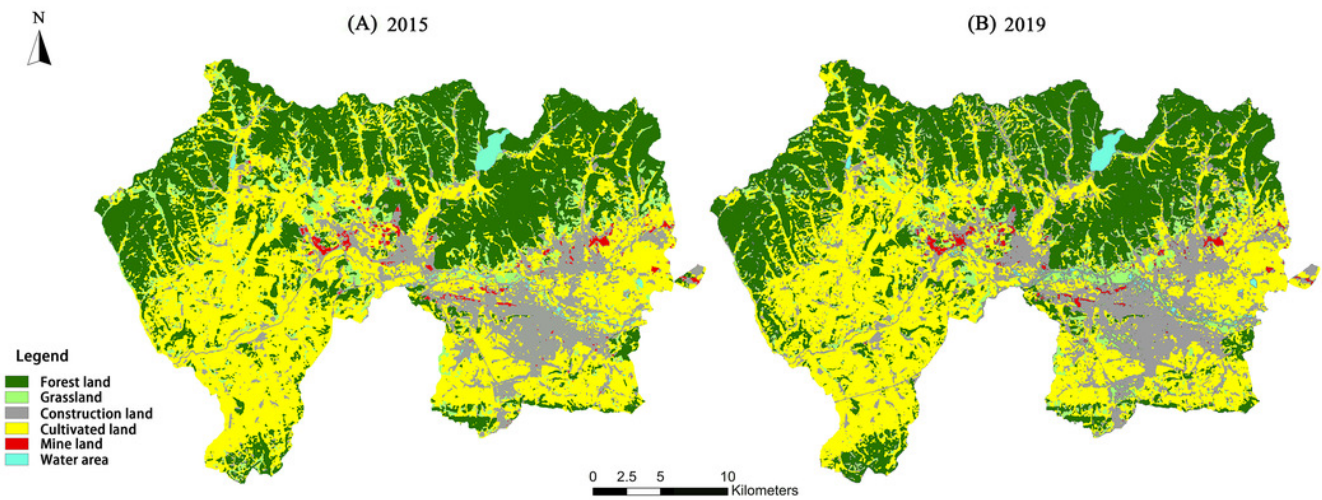


Figure 5

Figure 5 Vegetation coverage of the study area in 2015 and 2019

Vegetation coverage for (A) 2015, (B) 2019 of the three districts in Jixi, Heilongjiang, China.

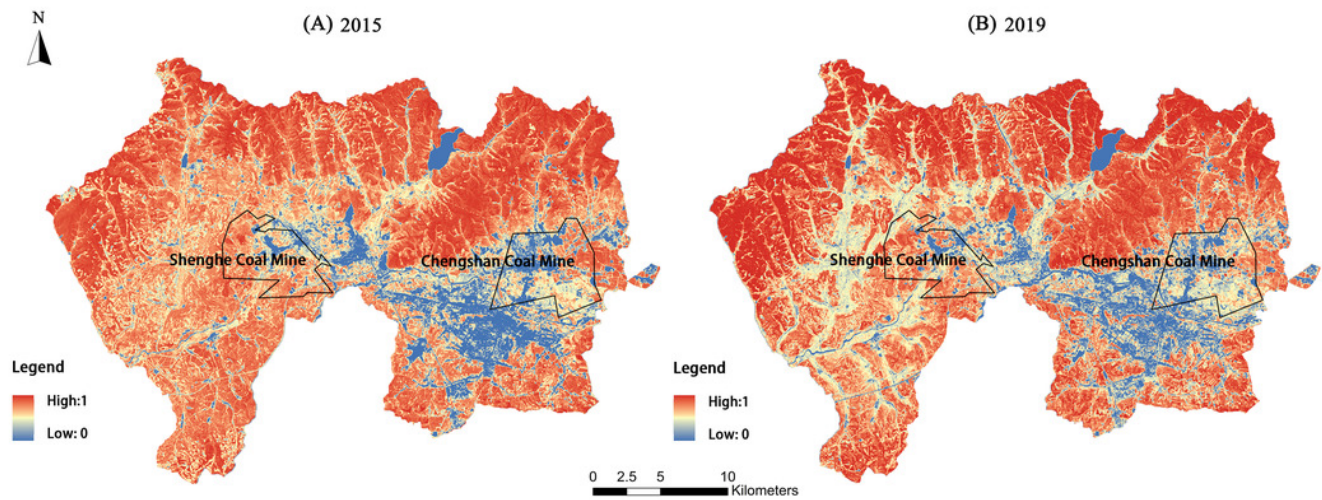


Figure 6

Figure 6 Variation in land surface temperature (LST) and vegetation coverage in pixel groups (1-56) along an E-W profile

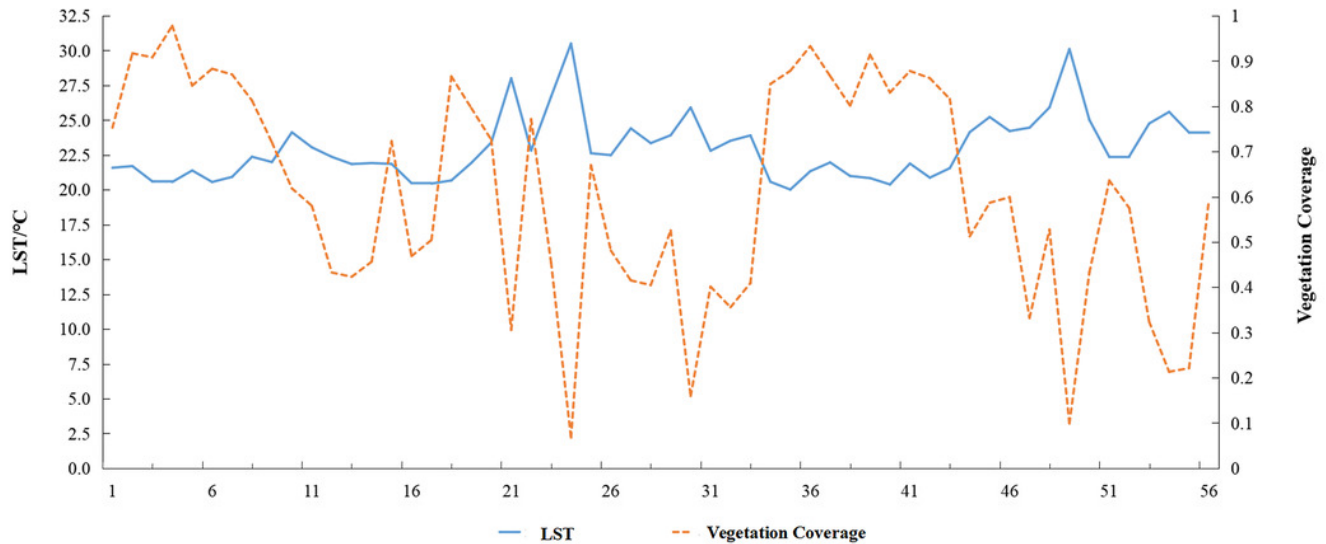


Figure 7

Figure 7 Correlation between land surface temperature (LST) and vegetation coverage of the study area

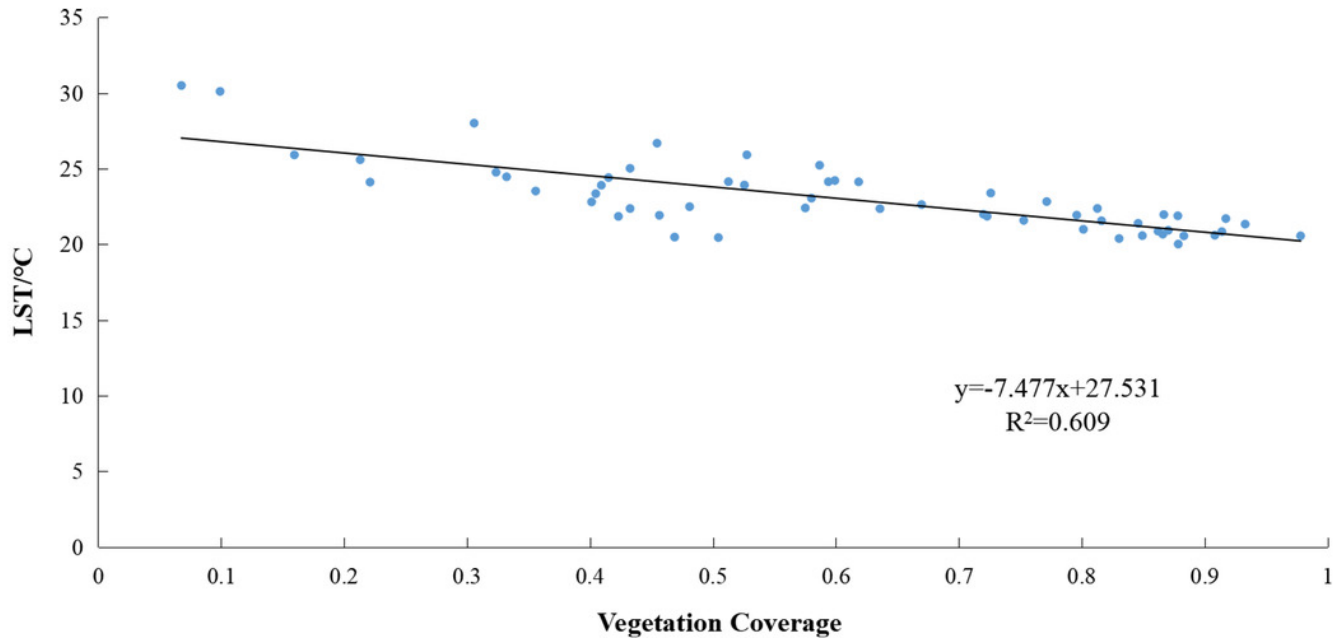


Figure 8

Figure 8 Correlation between patch area and average patch temperature of mining lands

LST, land surface temperature

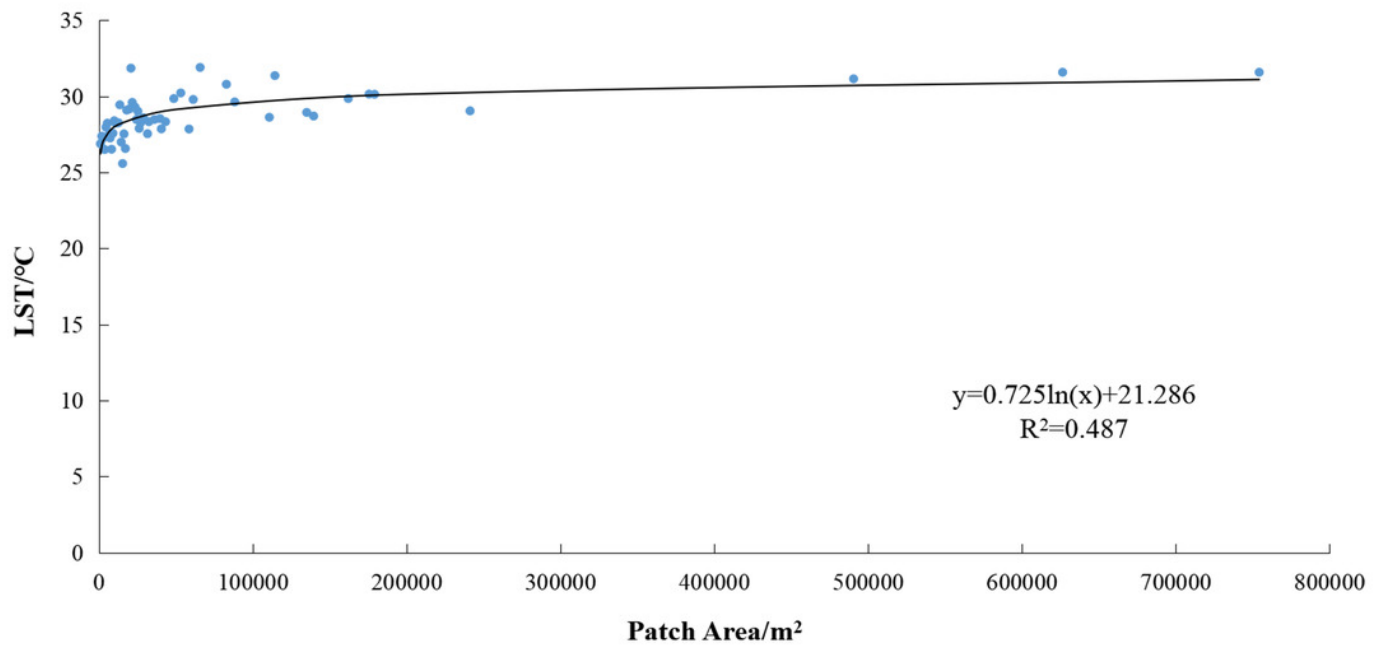


Figure 9

Figure 9 Correlation between patch area and maximum patch temperature of mining lands

LST, land surface temperature

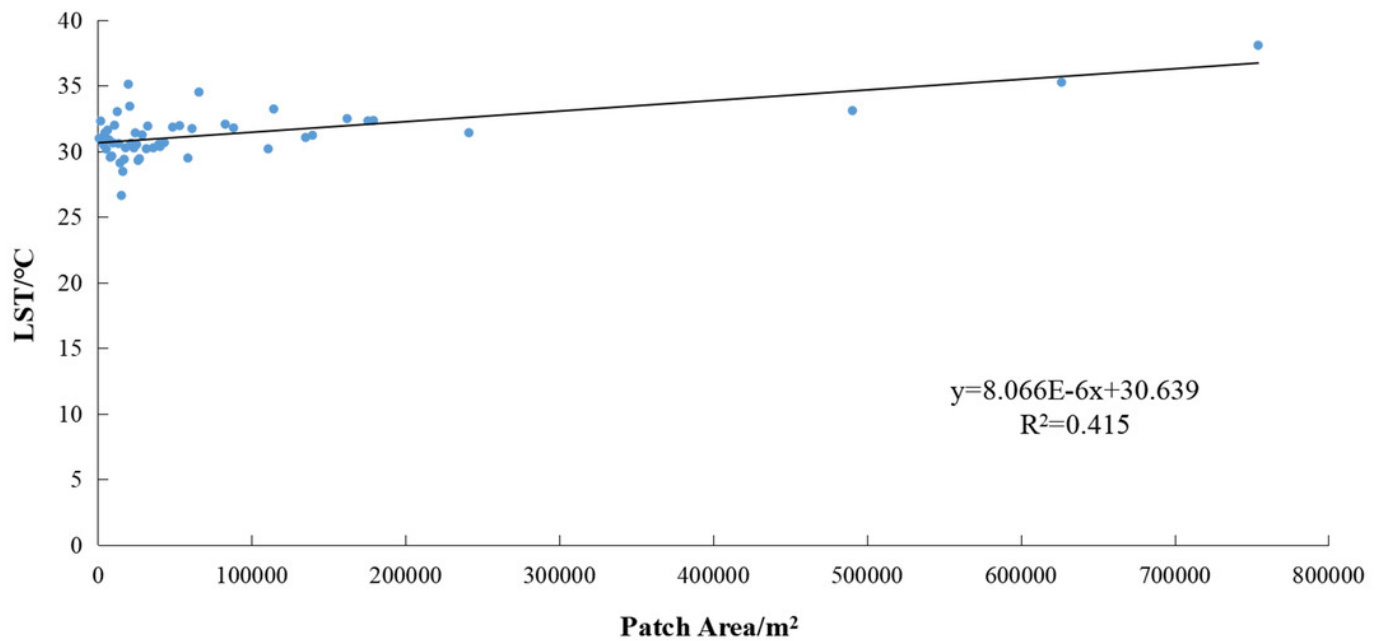


Figure 10

Figure 10 Schematic diagram of buffer zone in mining land patch

The legend has been noted in the figure.

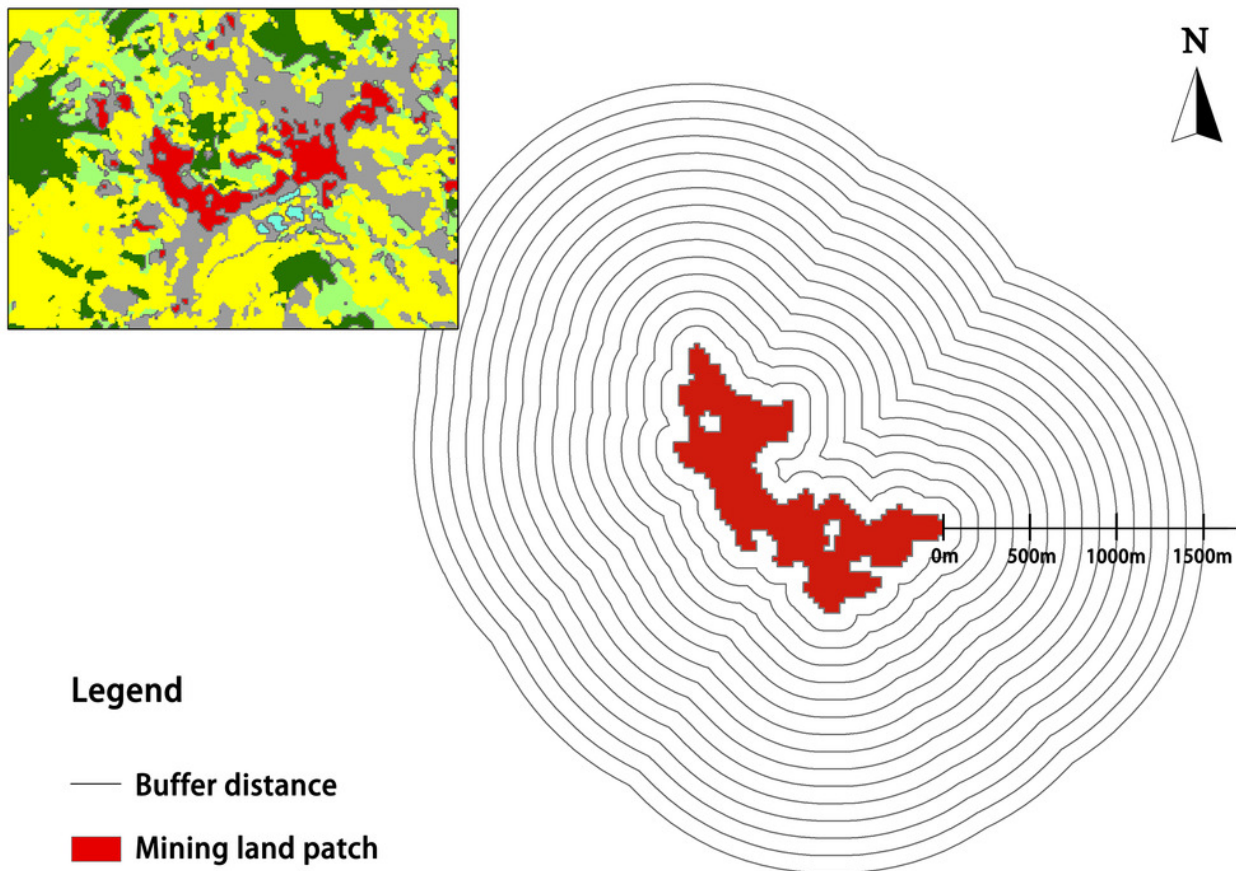


Figure 11

Figure 11 Variation of land surface temperature (LST) with buffer zone of mining lands

The double line on the coordinate axis represents the omitted part of the value, so the Y-axis can more clearly reflect the trend of the four sets of data in the figure.

